Hierarchical Hollow Bimetal Oxide Microspheres Synthesized through a Recrystallization Mechanism for High-Performance Lithium-Ion Batteries

Fanggang Li,[a] Maojun Zheng,*[a, b] Yuxiu You,[a] Dongkai Jiang,[a] Hao Yuan,[a] Zhihao Zhai,[a] Wenlan Zhang,[a] Li Ma,[c] and Wenzhong Shen[a, b]

Bimetal oxide with its intricate nanostructure holds great potential for high-performance electrode materials in lithium-ion batteries (LIBs). Herein, a facile strategy for the fabrication of hierarchical hollow $Co_3O_4/ZnCo_2O_4$ microspheres is developed, involving a simple solvothermal synthesis and subsequent thermal annealing in air. An aggregation-dissolution-in situ recrystallization structure evolution and growth mechanism is proposed. Benefiting from the unique hierarchical hollow structure with rational porosity, synergistic effect of bimetal components, and better electrical conductivity, the as-synthesized $Co_3O_4/ZnCo_2O_4$ hierarchical hollow microstructure shows outstanding lithium storage properties. As a result, a superior rate capability (842 mA h g^{-1} at a current density of 4 A g^{-1}) and an excellent cycle life (754 mA h g^{-1} after 800 cycles at a current density of 2 A g^{-1}) are obtained. The presented strategy could be applicable to the synthesis of mixed metal oxide hierarchical hollow structures with rational porosity for high-performance LIBs.

1. Introduction

Rechargeable lithium-ion batteries (LIBs) are widely used in portable electronic devices, electric vehicles, and have great application prospects in the large-scale storage of renewable energy.[1–2] However, the existing commercial graphite anodes provide a theoretical capacity of 372 mA h g^{-1}, which restricts the demand for large-scale use of LIBs. Therefore, it is highly desirable to develop suitable anode materials with high rate performance and long cycle life. Among the investigated materials, transition metal oxides are considered as the preferred substitution materials owing to their high reversible theoretical capacity, especially the cobalt oxide (Co_3O_4),[3–4] which possesses a high theoretical capacity of 890 mA h g^{-1}. Nonetheless, the low rate performance and poor cycle stability caused by low electrical conductivity and severe volume expansion hinder their applications. Several mixed bimetal oxides have been proposed to solve these problems owing to their synergy and complementary behavior, such as $CoMo_2O_4$,[5–6] $NiCo_2O_4$,[7] and $MnCo_2O_4$.[8] In particular, $ZnCo_2O_4$ has been considered as a competitive option because of its unique crystal structure (isostructural to Co_3O_4) and a special individual component that contributes to the electrochemical reaction mechanism (alloying-dealloying process: $Zn + Li^+ + e^- \leftrightarrow LiZn$).[9]

In addition to the chemical components of the material, a rational-designed structure is another key factor to achieve a high energy storage performance. Hierarchical nanostructures consisting of nanoparticles,[10–11] nanorods,[12] and nanosheets[13–14] can shorten the diffusion path of Li-ions and increase the interface area between the electrode and electrolyte, favoring a capacity improvement. Mainly, interconnected nanoparticle subunits promote the generation of voids, which can alleviate the structural stress and buffer the volume variation.[13,15] Besides, constructing hollow structures are another effective strategy,[16–19] providing sufficient contact between the inner part of the electrode and electrolyte, and extra free volume. For example, Guo's group reported the synthesis of hierarchical hollow $ZnCo_2O_4$ nanocages assembled from nanosheets by the etching of Cu_2O templates. The as-prepared hierarchical hollow nanocages exhibit a better cycle performance compared with conventional $ZnCo_2O_4$ nanoparticles.[18] Also, as demonstrated by Ru's group, one-dimensional (1D) porous $ZnCo_2O_4$ cuboids exhibit enhanced lithium storage properties of 724 mA h g^{-1} at a current density of 4 A g^{-1} using a micro-emulsion stratagem, which is considered to be a favorable morphology.[17] Despite the described advances, it is still highly necessary and quite challenging to develop facile and effective strategies for preparing hierarchical hollow bimetal oxides microspheres with rational porosity.

Herein, we report the synthesis of hierarchical hollow microspheres composed of $Co_3O_4/ZnCo_2O_4$ (ZCO) nanoparticles *via* a facile solvothermal method followed by a thermal

[a] Dr. F. Li, Prof. M. Zheng, Dr. Y. You, D. Jiang, H. Yuan, Z. Zhai, W. Zhang, Prof. W. Shen
Key Laboratory of Artificial Structures and Quantum Control (Ministry of Education), School of Physics and Astronomy
Shanghai Jiao Tong University
Shanghai 200240, P.R. China
E-mail: mjzheng@sjtu.edu.cn
[b] Prof. M. Zheng, Prof. W. Shen
Collaborative Innovation Center of Advanced Microstructures
Nanjing University
Nanjing 210093, P.R. China
[c] Prof. L. Ma
School of Chemistry and Chemical Technology
Shanghai Jiao Tong University
Shanghai 200240, P.R. China

Supporting information for this article is available on the WWW under https://doi.org/10.1002/celc.202000781

decomposition process. As schematically illustrated in Figure 1, initially, in step 1, ZnCo-carbonate microspheres are synthesized via a solvothermal method using urea as the precipitant, as well as different molar ratios of $CoCl_2$ and $ZnCl_2$ as metal sources. Later, in step 2, the precursors are calcined at different heating rates under an air atmosphere to form the final products. When investigated as anode materials for LIBs, the as-synthesized ZCO-0.5 hierarchical hollow microspheres exhibit superior rate capability and ultralong cycle life.

2. Results and Discussion

The crystallographic structures were first characterized by XRD to identify their chemical composition. As shown in Figure 2a, all of the diffraction peaks of the ZCO-0.5-carbonate can be indexed to $ZnCO_3$ and $CoCO_3$ (JCPDS card no. 83–1765 and no.78-0209). After annealing, the identified peaks of ZCO-0 (Figure 2b) are consistent with Co_3O_4 (JCPDS card No.74-2120). The schematic crystal structure of $ZnCo_2O_4$ is demonstrated in Figure 2d. It has a normal spinel structure with oxygen anions stacked in closed cubic patterns, Zn^{2+} located in one-eighth of the tetrahedral sites and the Co^{3+} sitting in half of the octahedral sites.[3] This crystal structure is isostructural to Co_3O_4

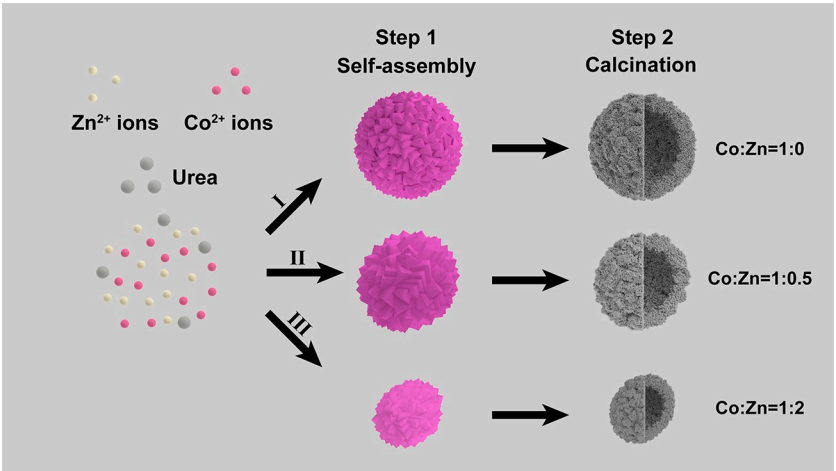

Figure 1. Schematic illustration of the synthesis procedure for hierarchical hollow ZCO microspheres.

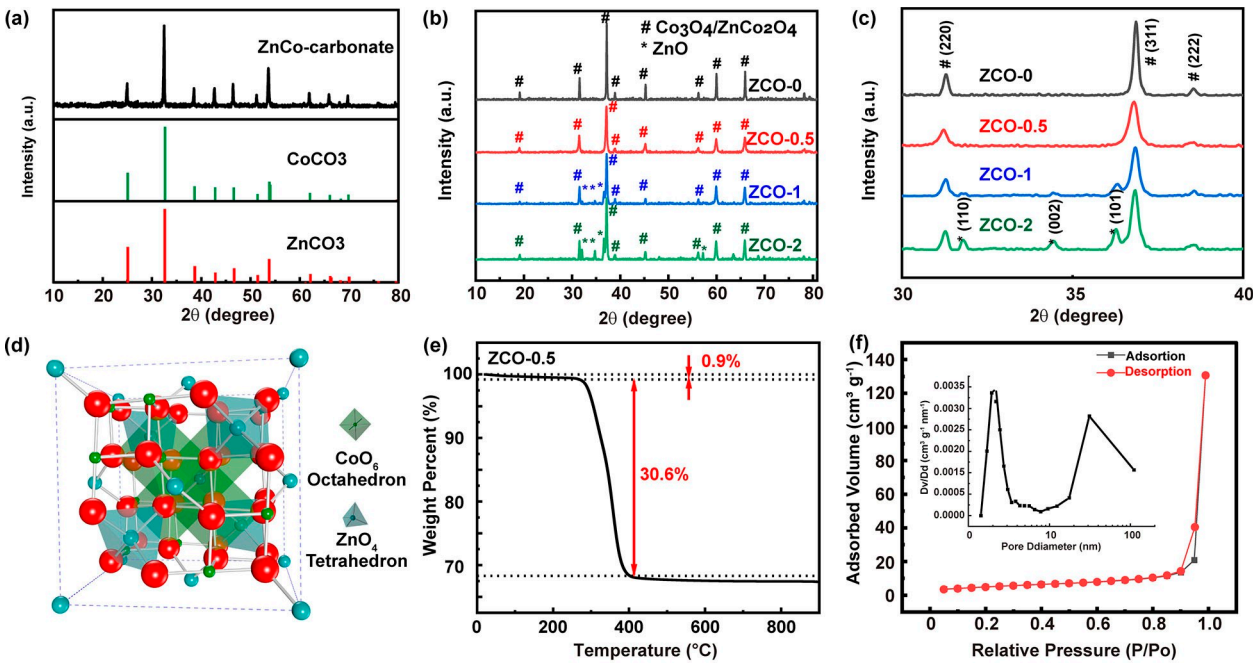

Figure 2. a) XRD diffraction pattern of ZnCo-0.5-carbonate. b) XRD diffraction patterns and c) (110), (002) and (101) diffraction peaks of ZnO for ZCO-x. d) Crystal structure of $ZnCo_2O_4$. e) TGA curves under air atmosphere of ZCO-0.5. f) N_2 adsorption-desorption isotherms and corresponding pore size distribution (inset) of ZCO-0.5.

(Figure S1). The diffraction peaks of ZCO-0.5 (Figure 2b) can be well indexed to a mixed phase of Co_3O_4 (JCPDS card No.74-2120) and $ZnCo_2O_4$ (JCPDS card No.23-1390), without additional impurity diffraction peaks from ZnO. Meanwhile, as the ratio of Zn/Co increases, ZnO peaks start emerging (Figure 2c ZCO-1) and become obvious (Figure 2c ZCO-2). ICP-OES was used to further verify the ratio of Co_3O_4 and $ZnCo_2O_4$ in ZCO-0.5, and the molar ratio of Co to Zn is 5.94. According to the XRD data, no ZnO is found in ZCO-0.5, indicating that all of the Zn ions are derived from $ZnCo_2O_4$. Therefore, ZCO-0.5 is composed of 56.5 % Co_3O_4 and 43.5 % $ZnCo_2O_4$. TGA was used to characterize the thermal behavior of the ZnCo-carbonate. As exhibited in Figure 2e two distinct processes of mass reduction were observed. The one before 300 °C is mainly caused by the evaporation of moisture adsorbed on the surface, while the main weight loss between 300 and 400 °C is due to the decomposition reactions of ZCO-carbonate to $ZnCo_2O_4$ and Co_3O_4.[20] As shown in Figure 2f and S2, the pore structure of ZCO-x was further investigated by N_2 adsorption-desorption measurements. The sorption isotherm is a type IV isotherm at the relative pressure range of 0.9–1.0 P/P_0.[11] ZCO-0.5 possesses the largest surface area (17.96 $m^2 g^{-1}$) and the smallest pore diameter (2.10 nm) compared with others using the BET method and BJH model. More detailed BET and Langmuir specific surface area and pore size data are given in Table 1. As the Zn/Co ratio gradually increases from 0.5 to 2, the pore size also gradually increases, which is consistent with the SEM image below.

Table 1. Specific surface area and pore size data for ZCO-x.

ZCO-x	Surface Area Multi BET [$m^2 g^{-1}$]	Langmuir [$m^2 g^{-1}$]	Pore Size Average [nm]	BJH [nm]
0	8.44	13.64	13.16	2.18
0.5	17.96	28.57	45.11	2.10
1	11.13	18.08	44.06	3.41
2	11.60	18.38	56.94	3.42

SEM images of the ZnCo-carbonate precursors in Figure 3a exhibit a solid and uniform sphere structure. Radially smooth cubic sub-micro-particles can be found by the higher magnification SEM image in Figure S3a. Notably, these structures are thermally stable so that after calcination, the original frameworks were still maintained (Figure 3b-h). A hollow structure with a wall thickness of about 1 μm, providing efficient space to reduce the volume variation during the electrochemical reaction, can also be observed from Figure 3c. The higher magnification image in Figure 3d shows the numerous nano-porous and primary nanoparticles with a diameter of about 50 nm. This mainly results from the CO_2 evolution during the decomposition of the precursor component, as well as crystallization during the annealing process. Additionally, this nano-microstructure with a high surface area providing full contact between the electrode and electrolyte offers more active sites for Li storage. The formation of such a hierarchical structure during the calcination process is due to the heterogeneous shrinkage by non-equilibrium heat treatment. With the heating rate of 4 °C min^{-1}, a temperature gradient (ΔT) along the radial direction of the carbonate spheres is expected. Due to the presence of ΔT, the outermost of the carbonate spheres decompose first, forming $ZnCo_2O_4/Co_3O_4$ shell structure. This structure can prevent the further shrinking of the outer diameter. The internal carbonate sphere continues to shrink, so the heterogeneous shrinkage occurs. Therefore, two forces in opposite directions are encountered between the inner core and the outer shell: cohesive force (σ_c) form the inner core and the adhesive force

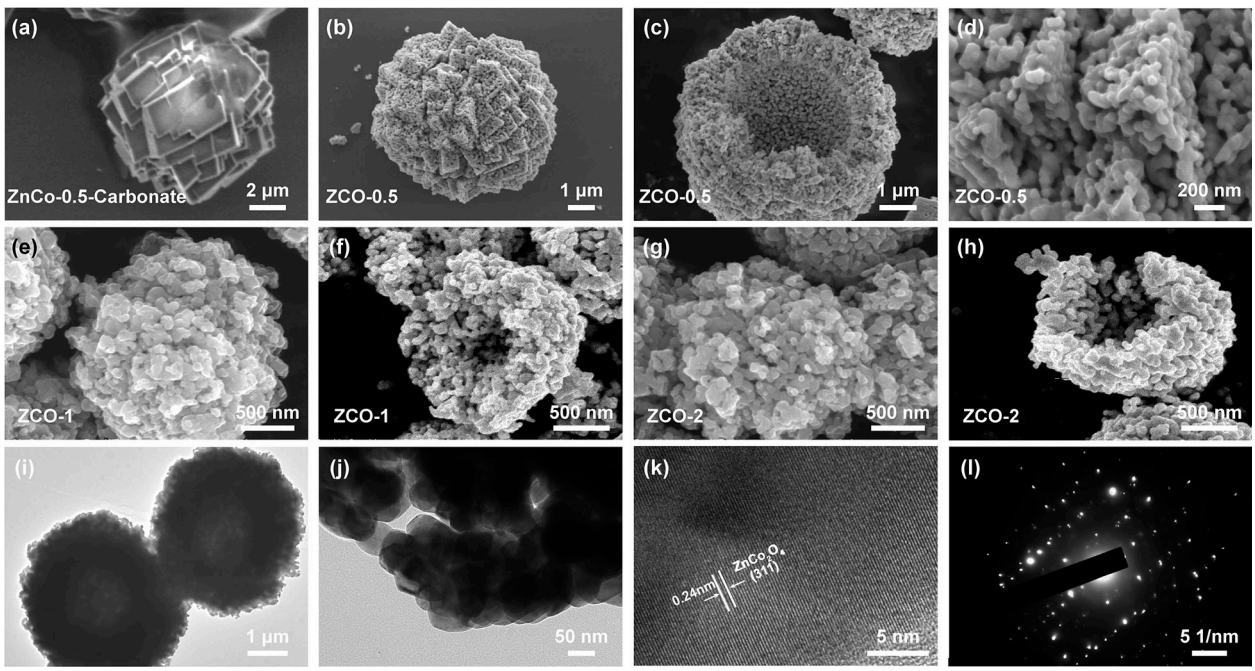

Figure 3. a) SEM images of ZnCo-0.5-carbonate, b–d) ZCO-0.5, e, f) ZCO-1 and g, h) ZCO-2. i–k) TEM and HRTEM images and l) SAED pattern of ZCO-0.5.

(σ_a) from the rigid shell. The former promotes the continued contraction of the core, while the latter prevents inward contraction. When $\sigma_c < \sigma_a$, the core gradually shrinks outward to the shell, thus forming this hollow structure.[16,21] As the Zn/Co ratio gradually increases from 0 to 2, the spheres turn into smaller ellipsoids, while the nanoparticles unit becomes larger (Figure 3e-h and S4). Because of the relatively easy nucleation of the zinc-based matrix during the bimetal coprecipitation process, as the content of Zn increases, the probability of zinc nucleation becomes larger, and the nucleation speed of zinc becomes faster.[22–23] Thus, the spheres turn into ellipsoids and become smaller, while the nanoparticles unit becomes larger. These hollow and porous structures are favorable for not only improving the interfacial contact between the electrode and electrolyte but also alleviating the volume expansion of the electrode during the charge and discharge process. Meanwhile, the nanosized particles can provide shorter paths for electron transportation and Li^+ diffusion. The detailed structural features of ZCO-0.5 were further characterized by TEM. Figure 3(i and j) presents the images of the hollow structure, which has a diameter of about 6 μm and consists of many discrete nanoparticles with a size of around 50 nm. This result is in accordance with the result calculated using the Scherrer equation[24–27] (Table S1). Besides, the diffraction spots displayed by the SAED patterns in Figure 3l prove that the microspheres consist of crystalline nanoparticles. The HRTEM image in Figure 3k shows interplane spacings of 0.24 and 0.27 nm, corresponding to the (311) and (220) planes of $ZnCo_2O_4$, respectively.

To more deeply understand the formation mechanism of the uniform spheres created by the smooth cubic sub-microparticle structures, a series of experiments with different reaction times were also performed. Figure 4 shows the TEM images under different reaction time conditions (40, 45, 50, 55 and 60 min), revealing an evolutionary process. At first, nanosheets form (Figure 4a and b) and aggregate to flower-like spheres (Figure 4c and d), which then become more significant (Figure 4e). Subsequently, the nanosheets expand (Figure 4f and g), cubic particles are generated and grow *in-situ* (Figure 4h and i), and, finally, stack into a uniform sphere. The crystal structure changes during this evolution process were analyzed by XRD (Figure S5). The nanosheets and nanoflower-like spheres have strong diffraction peaks around 10°, which is the characteristic peak of metal glycerol carbonate.[28] The reaction of glycerol with urea proceeds slowly under low temperature and without the catalyst. As the reaction proceeds, polymeric monoglycerolate complexes of zinc and cobalt can act as homogeneous catalysts to promote the synthesis of glycerol carbonate.[29–31] Thus, the nanosheets gradually expand and become porous. As the reaction time increases, $ZnCO_3$ and $CoCO_3$ peaks appear with the appearance of the cubic particles. This result means that as the reaction temperature increases, the carbon dioxide produced by the decomposition of urea forms more carbonates, which can continue growing in situ in

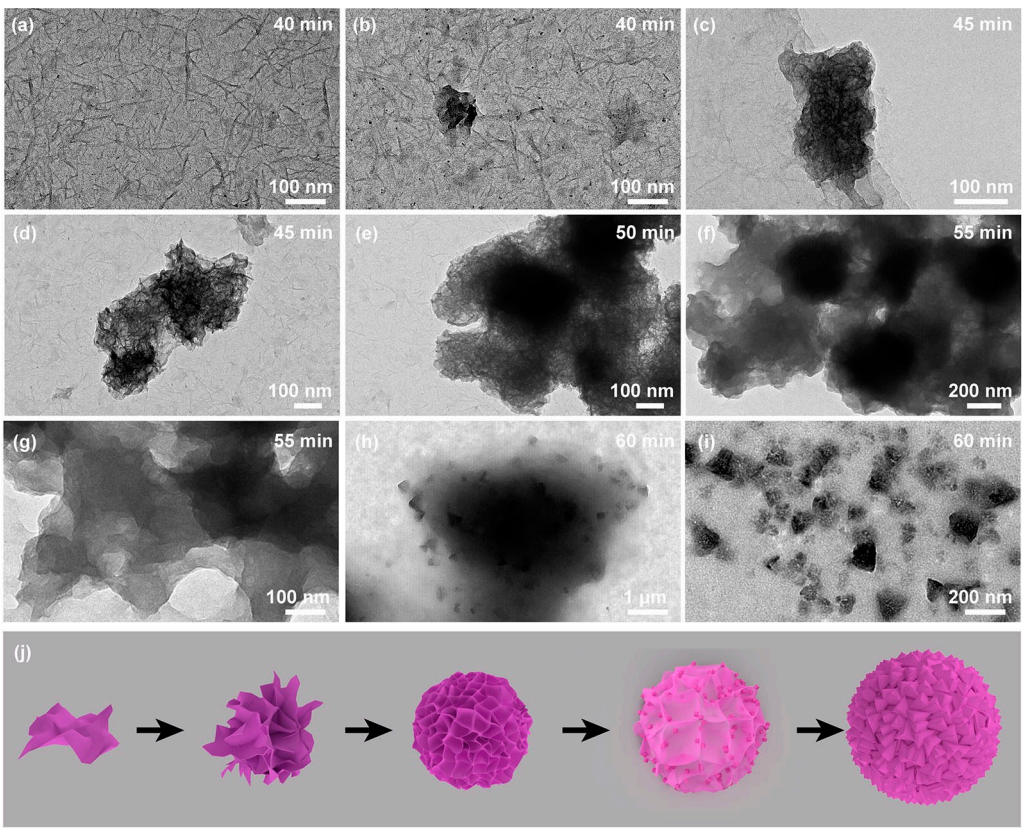

Figure 4. TEM images of the ZnCo-carbonate precursors under different reaction time conditions: 40 min (a, b); 45 min (c, d); 50 min (e); 55 min (f, g); 60 min (h, i). Schematic illustration of the proposed aggregation-dissolution-in situ recrystallization growth mechanism (j).

the nucleated part. This morphological evolution and phase structure transformation process are different from those of other works previously reported.[15,32–33] Thus, we propose a growth process mechanism of aggregation-dissolution-*in-situ* recrystallization for conveniently understanding the formation of such microspheres. At the beginning of the reaction, the metal glycerol carbonate nanosheets are formed and then nucleated by oriented growth in order to achieve minimum interfacial energies. As the orientation growth continues, the initial nucleated structures self-assemble to form flower-like spheres. Afterward, the nanosheets gradually expand and become porous, followed by *in-situ* recrystallization of the metal carbonate cubic particles. Finally, a microsphere consisting of metal carbonate compound cubes with a smooth surface is formed. This new formation mechanism, including the aggregation-dissolution-*in-situ* recrystallization process, is schematically illustrated in Figure 4j.

The XPS spectra were obtained to investigate the surface electronic states and compositions. The survey spectra, as shown in Figure 5a, displays the peaks of Zn, Co, and O elements as well as C from the reference. The Zn 2p spectra contain two major peaks at ~1020.6 and ~1043.6 eV (Figure S6a), assigned to Zn $2p_{3/2}$ and Zn $2p_{1/2}$ of Zn^{2+}, respectively.[34] In the case of Co 2p spectra, Figure S6b shows two main peaks at ~779.1 and ~794.1 eV, corresponding to the orbits of Co $2p_{3/2}$ and Co $2p_{1/2}$ peaks, respectively. And a spin-orbit splitting of around 15.0 eV, confirming the existence of mixed Co^{2+} and Co^{3+}.[35] Two additional weak satellite peaks are also observed at ~789 eV and ~804 eV, and the energy gap is around 10 eV between the main peak and the satellite peaks, further indicating the existence of Co^{3+}.[36] In terms of the fitting peak of $Co2p_{3/2}$ peaks in Figure 5c, the relative atomic ratio of Co^{3+}/Co^{2+} increase significantly from 2.04, 3.47, 4.55 to 5.21. The ratio of 3.47 indicates that ZCO-0.5 comprises $ZnCo_2O_4$ (42.7%) and Co_3O_4 (57.3%), coinciding with ICP-AES result (Detailed calculation results are in the Supporting Information on the bottom of Figure S6). The O 2p spectrum (Figure 5d) is deconvoluted into three peaks at 533.57, 530.78 and 529.71 eV, which are denoted as Oa (caused by the physically adsorbed oxygen), Od (mainly assigned to the defect sites), and Ol (associated with the lattice oxygen in the spinel $ZnCo_2O_4$ phase and Co_3O_4 phase), respectively.[9,37] It is worthwhile mentioning that the relative percentages of Od are about 27.59%, 35.82%, 32.68%, and 30.67%, respectively. Thus, ZCO-0.5 has much more defect sites than others, which would provide more active sites to promote the transport of lithium ions.[13]

The electrochemical performances of the as-synthesized samples were first evaluated by the CV test. Figure 6a gives the first CV curve of ZCO-0, 0.5, 1and 2. The first cathodic cycle of ZCO-0.5, 1 and 2 show the significant irreversible reduction peaks at ~0.87 V, consistent with the decomposition process of the $ZnCo_2O_4$ and Co_3O_4 to metallic Zn and Co (Eq. 1, 2),[34] while the peak moves to ~1.1 V in the next cycle, manifesting a different reaction pathway has occurred (Eq. 5, and 6). As the Zn content increases, a weak cathode peak locating at 0.46 V (ZCO-1) starts to appear and moves to 0.40 V (ZCO-2). This peak has not been detected in the later cycles under all conditions, indicating the reaction of Eq. 4 has occurred for the first cycle. Besides, the anode peak recorded at 2.07 V can be ascribed to the reaction of Eq. 5 and 6, while another peak recorded at ~1.70 V, attributed to the reversible reaction of Eq. 3, began to appear and strengthen as the content of Zn increases.[38] Figure 6b, c and S7 show the first three CV curves of ZCO, which are almost overlapped starting from the second cycle, implying the excellent cyclic stability and reversibility of the electrochemical reactions. Reaction kinetics can be obtained from CV curves by analyzing the functional relationship between the peak current and the scan rate, $i = av^b$, where a and b are both

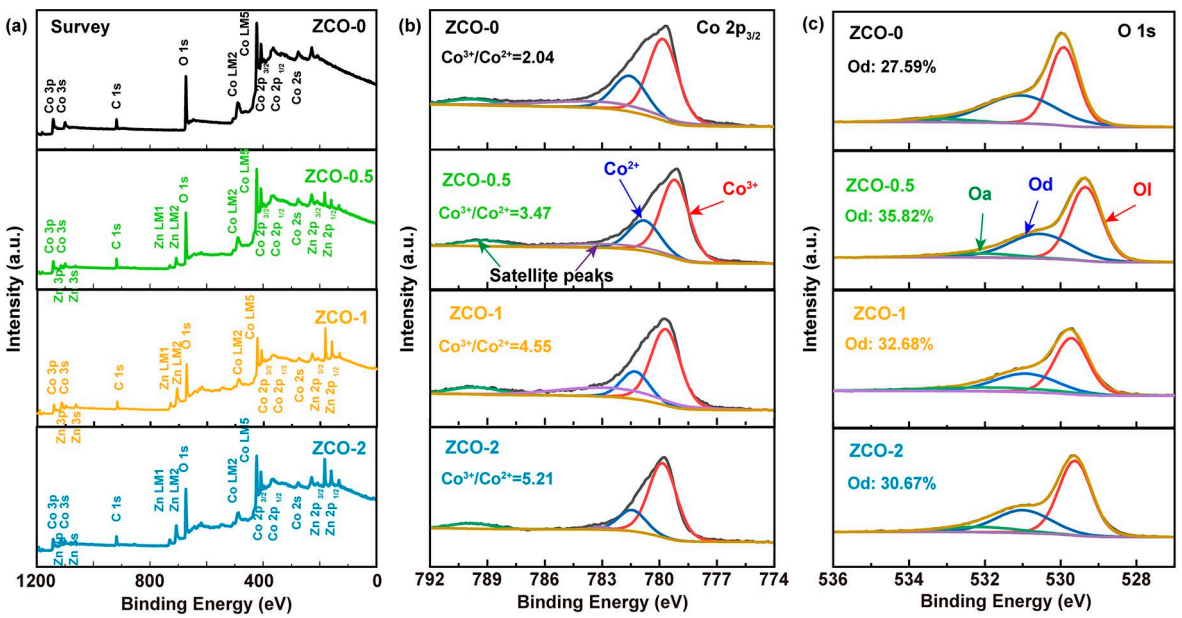

Figure 5. XPS spectra and fitting results of ZCO-x: a) survey spectra, b) Zn 2p, c) Co $2p_{3/2}$ and d) O 1s.

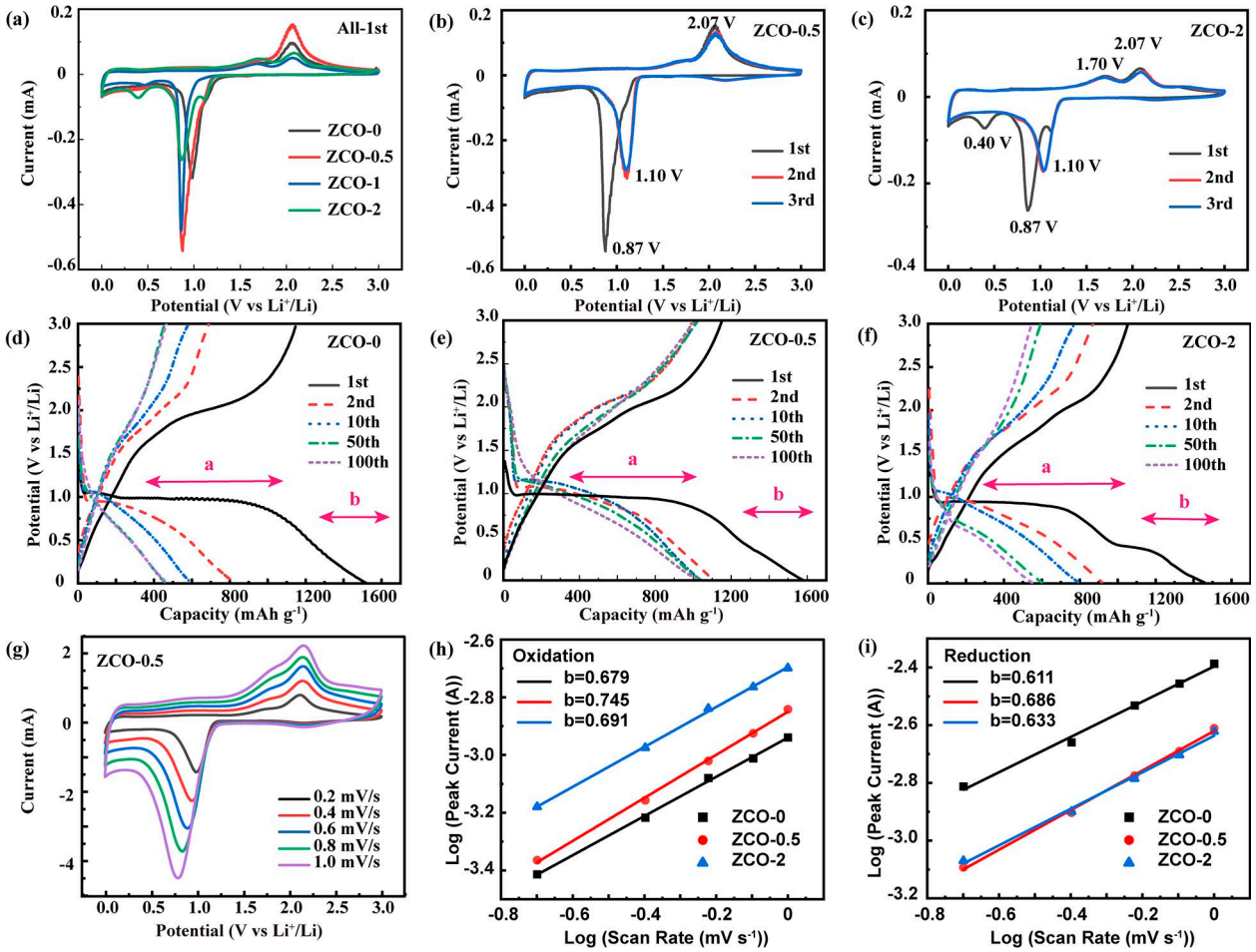

Figure 6. CV curves of a) 1st cycle plots of ZCO-x, b) the first three cycles of ZCO-0.5 and c) the first three cycles of ZCO-2 at a scan rate of 0.025 mV s^{-1} in the voltage window of 0.01–3.0 V. Galvanostatic discharge/charge cycling curves of d) ZCO-0, e) ZCO-0.5 and f) ZCO-2 at a current density of 1 A g^{-1}. g) CV curves of ZCO-0.5 at scan rates from 0.2 to 1.0 mV s^{-1}, h–i) relationship between the peak current and the scan rate.

constants. While b = 0.5 means a diffusion-controlled redox reaction is involved, and b = 1 indicates that a surface capacitive-controlled (pseudocapacitance) redox reaction is achieved. As shown in Figure 6g and S8, the linear fitted b value for the oxidation peaks are 0.679, 0.745, and 0.691, while for the reduction peaks are 0.611, 0.686, and 0.633, respectively. ZCO-0.5 possesses the maximum slope, suggesting a tendency for a surface capacitive-controlled mechanism. This result is consistent with the BET, SEM, and TEM analysis results, the small particles can provide more specific surface areas and thus increase the contribution of pseudocapacitance.

The electrochemical reactions can be clarified as follows in Equations (1)–(6):

$$ZnCo_2O_4 + 8Li^+ + 8e^- \rightarrow Zn + 2Co + 4Li_2O \quad (1)$$

$$Co_3O_4 + 8Li^+ + 8e^- \rightarrow 3Co + 4Li_2O \quad (2)$$

$$Zn + Li^+ + e^- \leftrightarrow LiZn \quad (3)$$

$$ZnO + 2Li^+ + e^- \rightarrow Zn + Li_2O \quad (4)$$

$$Co + Li_2O \leftrightarrow CoO + 2Li^+ + 2e^- \quad (5)$$

$$3CoO + Li_2O \leftrightarrow Co_3O_4 + 2Li^+ + 2e^- \quad (6)$$

The galvanostatic charge/discharge performance of ZCO-x electrode at 1 A g^{-1} are displayed in Figure 6d-f and S9. The first discharge profile shows a sudden decrease to 1.06 V followed by a plateau region "a" and finally a sloping region "b" in the voltage region from 0.90 to 0.01 V,[38] However, in the subsequent cycles, the plateau disappears, and a single slop is observed. The region "a" is the result of structure destruction or amorphization (Eq 1, 2), and region "b" is mainly caused by the inactivation of the inserted lithium-ion and the generation of SEI layer.[39] ZCO-0 and ZCO-0.5 are consisting of only one plateau region "a" at ~1.0 V, while ZCO-2 consisting a plateau region at ~1.0 V and a small plateau region at ~0.5 V, which can be ascribed to Eq. 4. This result is consistent with the CV analysis. The initial discharge and charge capacities of ZCO-0.5 are 1567 and 1173 mA h g^{-1}, respectively, with a low initial Coulombic Efficiency (CE) of 75%. Furthermore, the discharge and charge capacities of the 2nd, 10th, 50th, and 100th cycles are 1108/994, 1034/1007, 1037/1023, 1021/1008 mA h g^{-1}, respec-

tively, demonstrating the super stability of ZCO-0.5. Notably, all of them are higher than the theoretical capacities of $ZnCo_2O_4$ (903 mA h g^{-1}) and Co_3O_4 (890 mA h g^{-1}), and this phenomenon also occurs in other transition metal oxides, which is mainly ascribed to the synergistic effects of these reasons mentioned below: the formation of polymeric gel-like film on account of electrolyte degradation, the lithium-ion storage process at the interface and the presence of mesoporous structures.[21,40–41] It must also be mentioned that the initial CE for ZCO-0.5, 1, and 2 is 75%, 73%, and 72%, respectively. This decrease mainly results from the formation of SEI film caused by the existence of Zn. This phenomenon is in accordance with CV discussion.

The cycling performance of ZCO-0, 0.5, and 2 (Figure 7a) were firstly tested at a current of 1 A g^{-1} for 100 cycles. For the first cycle, all of the batteries are running at the current density of 100 mA g^{-1} to activate the electrode,[42–43] and the initial discharge capacities are 1535, 1568, and 1537 mA h g^{-1}, respectively. The second cycle discharge capacities are 985, 1105, and 927 mA h g^{-1}, respectively. After 100 cycles, ZCO-0.5 possesses the highest specific capacity of 1153 mA h g^{-1} (104.3% retention), while ZCO-0 and ZCO-2 only remain 398 mA h g^{-1} (40.4% retention) and 523 mA h g^{-1} (56.4% retention), respectively. Consequently, proper doping of Zn can significantly improve cycle stability.

The rate capability was evaluated at various current densities ranging from 0.2 to 4 A g^{-1} (Figure 7b). As expected, ZCO-0.5 reveals the best rate performance with the discharge capacity of 1042, 1045, 1014, 946, 842 mA h g^{-1} at current densities of 0.2, 0.5, 1, 2 and 4 A g^{-1}, respectively. Moreover, after the current density returns to 0.5 A g^{-1}, the specific capacity of ZCO-0.5 and 1 (recovers to1190 and 969 mA h g^{-1}) is even larger than before (1042 and 928 mA h g^{-1}), which is mainly due to the activation of the electrode.[44] It should be pointed out that as the ratio of Zn increases (from 0 to 2), the performance first gets better and then worsens. The reason for the better performance is that stable $ZnCo_2O_4$ significantly improves rate capability.[13,45] However, as the ratio further increases, the size of nanoparticles becomes larger, resulting in significant volume expansion and further deteriorating the rate performance.

To further prove the performance advantage of this sample, a high-rate and long-term cycle was carried out. Figure 7c shows that ZCO-0.5 still owns the highest retained capacity of 754 mA h g^{-1} after 800 cycles at current densities of 2 A g^{-1} than others. The coulombic efficiency is very close to 100% all over 800 cycles, which demonstrates good reversibility of the electrode. In comparison, the retained capacity of ZCO-0 and 2 are only 294 and 390 mA h g^{-1}, respectively. Another interesting finding is that the discharge capacity of ZCO-0.5 gradually decreases to 660 mA h g^{-1} in the first 200 cycles, and increases in the next 300 cycles step by step and maintain about 754 mA h g^{-1} after 800 cycles. Such phenomenon often occurs in some transition metal oxides as reported in previous literature.[15,46] Thus, this hierarchical hollow ZCO microsphere possesses excellent cycle performance and stability. To further confirm that ZCO-0.5 is the best choice, the cycling performance of ZCO-0.2 was tested at a current of 1 A g^{-1} and shown in Figure S10. After 100 cycles, ZCO-0.2 only possesses 762 mA h g^{-1}. This result further proves that ZCO-0.5 is the best choice. Besides, the SEM images of ZCO-x after 100 cycles at current density of 1 A g^{-1} are showed in Figure S11. The SEM images clearly illustrate that most of ZCO-0.5 retained the

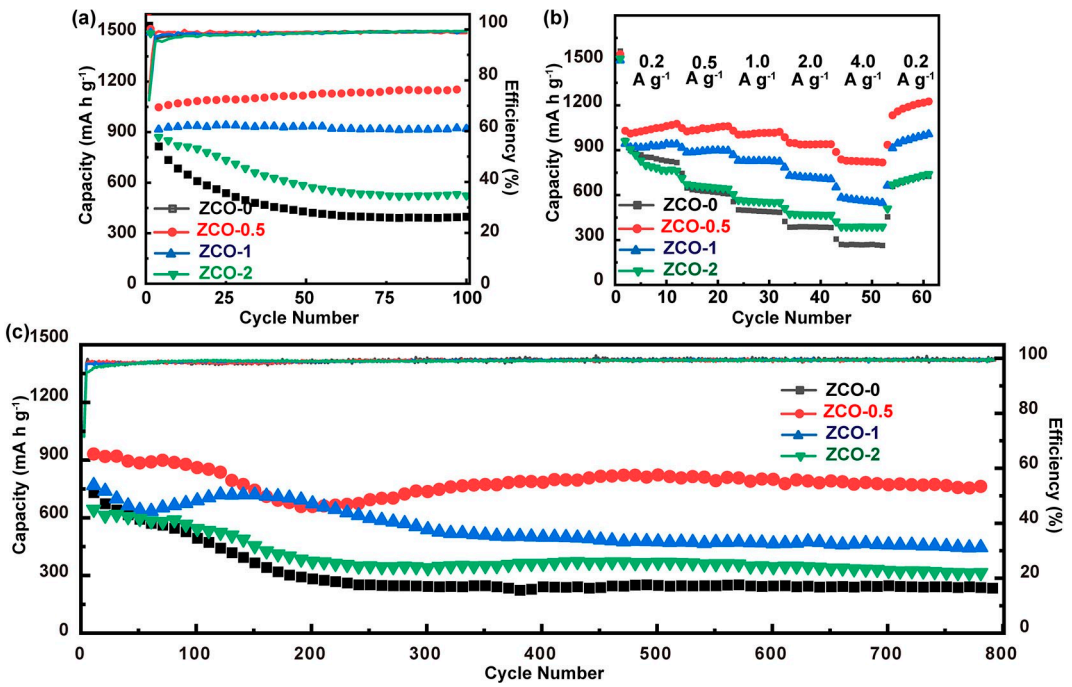

Figure 7. a) Cycling performance of ZCO-x at a current of 1 A g^{-1} accompanied with corresponding CEs. b) Rate performance of ZCO-x at various rates. c) Cycling performance of ZCO-x at a current of 2 A g^{-1} accompanied with corresponding CEs.

spherical structure so that it can maintain high stability during cycling. Only some of ZCO-0 and 1 kept the spherical structure, while ZCO-2 has completely collapsed without any spherical structure.

EIS was used to study the kinetic parameters, which consist of the mass transfer process in two phases and the charge transfer process in a two-phase interval. Figure 8(a) shows the equivalent circuit diagram, in which R represents the internal resistance caused by the electrode and electrolyte, Rct and CPE are the faradic charge transfer resistance and the double-layer capacitance, respectively, and W is the Warburg resistance.[47] The Nyquist plots of different samples before cycling are shown in Figure 8b, consisting of a semicircular segment at high frequency caused by Rct and CPE, and a slope segment at low frequency attributed to the existence of Warburg resistance. ZCO-0.5 has the smallest semicircle diameter compared with the others, indicating that it possesses a more stable surface film and faster charge transfer.[32] Meanwhile, Table S2 shows that ZCO-0.5 has a smaller Rct compared with ZCO-0, suggesting that the size of the nanoparticles and the synergism of the bimetals can simultaneously enhance conductivity. Nyquist plots of ZCO-0.5 with different cycle numbers were also tested and are shown in Figure 8c, and their fitting data are in Table S3. As the number of cycles increases, the internal resistance gradually increases (from 6.34 to 11.04 Ohm), which causes a decay in the capacity. In Figure 8d, σ is also calculated, which is inversely proportional to the square root of the diffusion coefficient. Impressively, there is no significant difference between the data of 100 cycles and 200 cycles, which means that the sample has excellent cyclic stability.[48]

Overall, the ZCO-0.5 exhibits outstanding lithium storage properties compared with the ZCO-0, 1, and 2, and many previously reported cobalt-based nanostructures (Table S4). The improved lithium storage performance of the hierarchical hollow microstructure ZCO could be attributed to the following reasons: first, the nanosized structural subunits and the synergism of the bimetal can simultaneously promote charge transfer at the electrode and electrolyte interface, ensuring excellent electrochemical activity. Second, the ZCO hybrid can integrate the high stability of $ZnCo_2O_4$ and high capacity of Co_3O_4 and improve the lithium storage performance. Furthermore, the unique hollow architecture with high porosity can increase the contact area between the electrode and electrolyte, as well as relieve volume expansion during cycles, exhibiting enhanced rate capability and cycling stability.

3. Conclusions

We fabricated a hierarchical hollow $Co_3O_4/ZnCo_2O_4$ microsphere with rational porosity, superior rate capability, and ultralong cycle life. Based on the morphology evolution and phase transformation process, we proposed an aggregation-dissolution-*in-situ* recrystallization growth mechanism. The nanoparticle subunits and the synergism of the bimetal simultaneously promote the electrical conductivity, which is verified by EIS analysis; the unique hierarchical hollow structure with high porosity relieves the volume expansion and increases the contact area between the electrode and electrolyte. Moreover, the mixture of Co_3O_4 and $ZnCo_2O_4$ inherits their advantages of higher capacity and higher stability, respectively. The as-prepared hierarchical hollow $Co_3O_4/ZnCo_2O_4$ microsphere exhibits outstanding lithium storage properties with a high capacity of 754 mA h g^{-1} at a current density of 2 A g^{-1} after 800 cycles as the anode materials for LIBs. This strategy can be easily applied to synthesize mixed metal oxides with hierarchical hollow structures.

Experimental Section

Material Preparation

ZnCo-carbonate precursors were synthesized through a modified solvothermal method. In brief, 8 g of urea, 0.875 g of $CoCl_2 \cdot 6H_2O$, and different masses of $ZnCl_2 \cdot 6H_2O$ (0, 0.251, 0.502, and 1.004 g) were dissolved into a solution with 17.5 mL of H_2O and 52.5 mL of

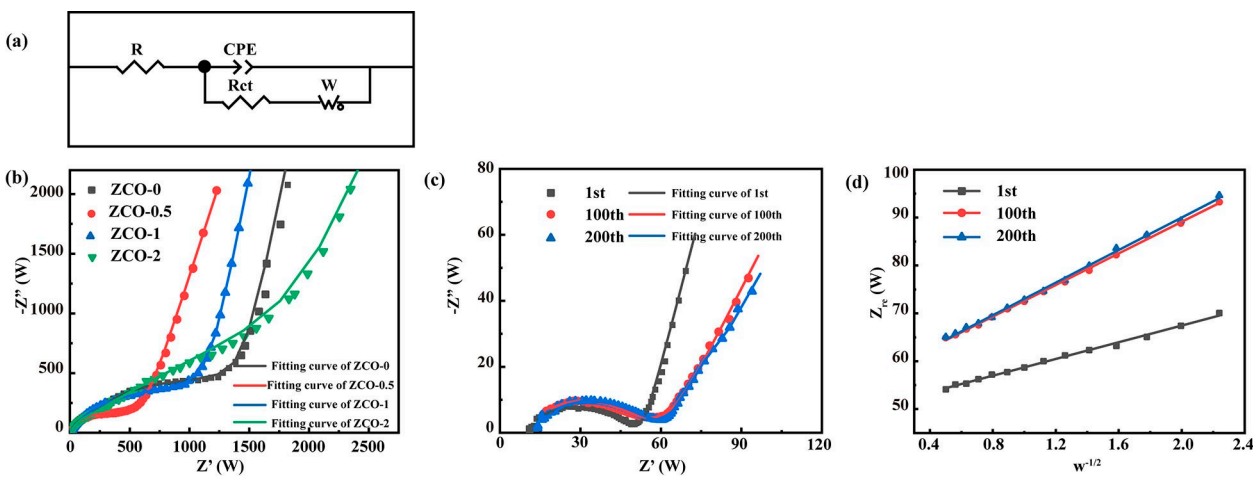

Figure 8. a) Equivalent circuit model. b) Nyquist plots of ZCO-x before cycling. c) Nyquist plot of Zn–Co-0.5 after different cycles. d) The linear relationship between Zre and $\omega^{-1/2}$.

glycerol at room temperature under stirring. After being stirred for 1 h, the solution was transferred into a 100 mL Teflon-lined stainless-steel autoclave, which was sealed and gradually heated to 180 °C for 12 h. After cooling to room temperature, the obtained precursors were washed with DI water and ethanol several times and dried at 80 °C overnight. Finally, the obtained composites, after being calcined in air at 600 °C for 3 h with a heating rate of 4 °C/min, were labeled as ZCO-0, ZCO-0.5, ZCO-1, and ZCO-2. Experiments using different molar ratios of Zn/Co (0, 1, and 2) were also synthesized with the same method.

Material Characterization

Scanning electron microscopy (SEM) images were obtained using a Sirion 200. Transmission electron microscopy (TEM), high-resolution transmission electron microscopy (HRTEM), and selected area electron diffraction (SAED) measurements were collected on a JEOL JEM-2100F with an acceleration voltage of 200 kV. X-ray diffraction (XRD) patterns were recorded on a Rigaku Ultima IV X-ray diffractometer with a Cu–Kα radiation source (10°/min from 10 to 80°). X-ray photoelectron spectroscopy (XPS) spectra were tested with an AXIS ULTRA DLD. Thermal gravimetric analyses (TGA) were measured using a Pyris 1 TGA under air atmosphere with a heating rate of 10 °C/min. Inductively coupled plasma optical emission spectrometry (ICP-OES) analyses were performed on an iCAP7600. The Brunauer-Emmett-Teller (BET) specific surface area and the analysis of the porosity were performed through measuring N_2 adsorption-desorption isotherms at 77 K using an Autosorb-IQ3.

Electrochemical Measurements

All of the cells were assembled using CR2016 coin-type half-cells in a glovebox with water/oxygen content lower than 0.5 ppm, and all of the electrochemical experiments were carried out at room temperature. The working electrodes were prepared by coating a paste containing 70 wt.% of the active material, 20 wt.% of acetylene black, and 10 wt.% of polyvinylidene difluoride (PVDF) onto a Cu foil and drying in a vacuum oven at 100 °C overnight. The average mass loading of the active material was about 0.8 mg. The electrolyte was 1 M $LiPF_6$ dissolved in an EC/DMC/EDC (1 : 1 : 1 wt.) solution. Lithium foil was used as the counter electrode. The galvanostatic charge/discharge tests were conducted on a LAND cycler in a voltage range of 0.01–3.0 V. Cyclic voltammetry (CV) measurements were performed at a scan rate of 0.025 mV s^{-1} with a voltage window of 0.01–3.0 V on a CHI 660D electrochemical workstation. Electrochemical impedance spectroscopy (EIS) data were recorded on a PARSTAT 4000 electrochemical workstation at a frequency range from 100 kHz to 0.01 Hz with an amplitude of 5 mV.

Acknowledgements

We gratefully acknowledge the support of this work by the National Natural Science Foundation of China (Grant no. 11174197, 11574203) and the support from the Instrumental Analysis Center of Shanghai Jiao Tong University.

Conflict of Interest

The authors declare no conflict of interest.

Keywords: hierarchical hollow structure · in situ recrystallization · $Co_3O_4/ZnCo_2O_4$ · lithium-ion batteries · anode materials

[1] M. Armand, J. M. Tarascon, *Nature* **2008**, *451*, 652.
[2] L. Yu, X. Y. Yu, X. W. D. Lou, *Adv. Mater.* **2018**, *30*, e1800939.
[3] F. F. Wu, J. Bai, J. K. Feng, S. L. Xiong, *Nanoscale* **2015**, *7*, 17211–17230.
[4] Y. M. Chen, L. Yu, X. W. Lou, *Angew. Chem. Int. Ed. Engl.* **2016**, *55*, 5990–5993.
[5] J. Xu, S. Z. Gu, L. Fan, P. Xu, B. G. Lu, *Electrochim. Acta* **2016**, *196*, 125–130.
[6] Y. Yang, S. Wang, C. Jiang, Q. Lu, Z. Tang, X. Wang, *Chem. Mater.* **2016**, *28*, 2417–2423.
[7] Y. Pan, W. J. Zeng, L. Li, Y. Z. Zhang, Y. N. Dong, D. X. Cao, G. L. Wang, B. L. Lucht, K. Ye, K. Cheng, *Nano-Micro Lett.* **2017**, *9*.
[8] X. Kong, T. Zhu, F. Cheng, M. Zhu, X. Cao, S. Liang, G. Cao, A. Pan, *ACS Appl. Mater. Interfaces* **2018**, *10*, 8730–8738.
[9] H. L. Xin, D. Z. Li, L. D. Shi, M. W. Ji, Y. M. Lin, J. L. Yu, B. Yang, C. H. Li, C. Z. Zhu, *Chem. Eng. J.* **2018**, *341*, 601–609.
[10] J. J. Deng, X. L. Yu, X. Y. Qin, B. H. Li, F. Y. Kang, *J. Alloys Compd.* **2019**, *780*, 65–71.
[11] Z. Wang, Q. Ru, X. Q. Chen, Q. Guo, B. Wang, X. H. Hou, S. J. Hu, *ChemElectroChem* **2017**, *4*, 2218–2224.
[12] W. B. Fu, Y. L. Wang, W. H. Han, Z. M. Zhang, H. M. Zha, E. Q. Xie, *J. Mater. Chem. A* **2016**, *4*, 173–182.
[13] J. Yu, Y. L. Wang, L. H. Mou, D. L. Fang, S. M. Chen, S. J. Zhang, *ACS Nano* **2018**, *12*, 2035–2047.
[14] F. Wang, F. Li, L. Ma, M. Zheng, *Chemistry* **2019**, *25*, 14598–14603.
[15] J. Bai, X. Li, G. Liu, Y. Qian, S. Xiong, *Adv. Funct. Mater.* **2014**, *24*, 3012–3020.
[16] L. Zhou, Z. Zhuang, H. Zhao, M. Lin, D. Zhao, L. Mai, *Adv. Mater.* **2017**, *29*.
[17] S. Cheng, Q. Ru, P. Liu, H. Yan, Z. Shi, X. Hou, S. Su, L. Zhao, F. Chi-Chung Ling, *J. Alloys Compd.* **2019**, *809*.
[18] B. H. Liu, H. Liu, M. F. Liang, L. X. Liu, Z. L. Lv, H. Zhou, H. Guo, *Nanoscale* **2017**, *9*, 17174–17180.
[19] X. Li, L. Chen, Y. Qu, Y. Ma, *Sustain Energ Fuels* **2018**, *2*, 1124–1140.
[20] X. Song, Q. Ru, Y. D. Mo, L. Y. Guo, S. J. Hu, B. N. An, *J. Power Sources* **2014**, *269*, 795–803.
[21] L. Huang, G. H. Waller, Y. Ding, D. C. Chen, D. Ding, P. X. Xi, Z. L. Wang, M. L. Liu, *Nano Energy* **2015**, *11*, 64–70.
[22] J. W. Choi, D. Aurbach, *Nat. Rev. Mater.* **2016**, *1*.
[23] Y. K. Sun, Z. Chen, H. J. Noh, D. J. Lee, H. G. Jung, Y. Ren, S. Wang, C. S. Yoon, S. T. Myung, K. Amine, *Nat. Mater.* **2012**, *11*, 942–947.
[24] S. M. Hwang, S. Y. Kim, J. G. Kim, K. J. Kim, J. W. Lee, M. S. Park, Y. J. Kim, M. Shahabuddin, Y. Yamauchi, J. H. Kim, *Nanoscale* **2015**, *7*, 8351–8355.
[25] S. M. Hwang, Y.-G. Lim, J.-G. Kim, Y.-U. Heo, J. H. Lim, Y. Yamauchi, M.-S. Park, Y.-J. Kim, S. X. Dou, J. H. Kim, *Nano Energy* **2014**, *10*, 53–62.
[26] J. Lee, J. Moon, S. A. Han, J. Kim, V. Malgras, Y. U. Heo, H. Kim, S. M. Lee, H. K. Liu, S. X. Dou, Y. Yamauchi, M. S. Park, J. H. Kim, *ACS Nano* **2019**, *13*, 9607–9619.
[27] H. Xue, J. Zhao, J. Tang, H. Gong, P. He, H. Zhou, Y. Yamauchi, J. He, *Chemistry* **2016**, *22*, 4915–4923.
[28] Y. Lu, J. Nai, X. W. D. Lou, *Angew. Chem. Int. Ed. Engl.* **2018**, *57*, 2899–2903.
[29] T. W. Turney, A. Patti, W. Gates, U. Shaheen, S. Kulasegaram, *Green Chem.* **2013**, *15*.
[30] M. Aresta, A. Dibenedetto, F. Nocito, C. Ferragina, *J. Catal.* **2009**, *268*, 106–114.
[31] S.-i. Fujita, Y. Yamanishi, M. Arai, *J. Catal.* **2013**, *297*, 137–141.
[32] W. X. Song, K. Y. Ji, A. Aguadero, P. R. Shearing, D. J. L. Brett, F. Xie, D. J. Riley, *Energy Storage Mater.* **2018**, *14*, 324–334.
[33] J. Bai, K. Q. Wang, J. K. Feng, S. L. Xiong, *ACS Appl. Mater. Interfaces* **2015**, *7*, 22848–22857.
[34] G. Y. Huang, Y. Yang, H. Y. Sun, S. M. Xu, J. L. Wang, M. Ahmad, Z. H. Xu, *J. Alloys Compd.* **2017**, *724*, 1149–1156.
[35] S. J. Hao, B. W. Zhang, S. Ball, M. Copley, Z. C. Xu, M. Srinivasan, K. Zhou, S. Mhaisalkar, Y. Z. Huang, *J. Power Sources* **2015**, *294*, 112–119.
[36] Y. You, M. Zheng, D. Jiang, F. Li, H. Yuan, Z. Zhai, L. Mac, W. Shena, *J. Mater. Chem. A* **2018**, *6*, 8742–8749.
[37] S. N. Xiao, D. L. Pan, R. Liang, W. R. Dai, Q. T. Zhang, G. Q. Zhang, C. L. Su, H. X. Li, W. Chen, *Appl. Catal. B* **2018**, *236*, 304–313.

[38] M. V. Reddy, K. Y. H. Kenrick, T. Y. Wei, G. Y. Chong, G. H. Leong, B. V. R. Chowdari, *J. Electrochem. Soc.* **2011**, *158*, A1423-A1430.
[39] Q. S. Xie, L. Lin, Y. T. Ma, D. Q. Zeng, J. R. Yang, J. Huang, L. S. Wang, D. L. Peng, *Electrochim. Acta* **2017**, *226*, 79–88.
[40] H. W. Liu, Q. H. Hu, *Nanotechnology* **2018**, *29*.
[41] Q. S. Xie, D. Q. Zeng, Y. T. Ma, L. Lin, L. S. Wang, D. L. Peng, *Electrochim. Acta* **2015**, *169*, 283–290.
[42] Y. Yang, S. Liu, X. Bian, J. Feng, Y. An, C. Yuan, *ACS Nano* **2018**, *12*, 2900–2908.
[43] Y. Wang, J. Li, S. Chen, B. Li, G. Zhu, F. Wang, Y. Zhang, *Inorg. Chem. Front.* **2018**, *5*, 559–567.
[44] X. Y. Hou, S. Bai, S. Xue, X. N. Shang, Y. J. Fu, D. Y. He, *J. Alloys Compd.* **2017**, *711*, 592–597.
[45] V. Aravindan, Y.-S. Lee, S. Madhavi, *Adv. Energy Mater.* **2015**, *5*.
[46] J. J. Deng, X. L. Yu, Y. B. He, B. H. Li, Q. H. Yang, F. Y. Kang, *Energy Storage Mater.* **2017**, *6*, 61–69.
[47] Q. Wu, J. Xu, X. Yang, F. Lu, S. He, J. Yang, H. J. Fan, M. Wu, *Adv. Energy Mater.* **2015**, *5*.
[48] Y. Ma, P. Liu, Q. Xie, G. Zhang, H. Zheng, Y. Cai, Z. Li, L. Wang, Z.-Z. Zhu, L. Mai, D.-L. Peng, *Nano Energy* **2019**, *59*, 184–196.

Manuscript received: June 8, 2020
Revised manuscript received: July 11, 2020
Accepted manuscript online: July 21, 2020